Editors' Suggestion

Wetting boundaries for a ternary high-density-ratio lattice Boltzmann method

Neeru Bala,[1] Marianna Pepona,[2] Ilya Karlin,[3,*] Halim Kusumaatmaja,[2,†] and Ciro Semprebon[1,‡]
[1]*Department of Mathematics, Physics and Electrical Engineering, Northumbria University, Newcastle upon Tyne NE1 8ST, United Kingdom*
[2]*Department of Physics, Durham University, Durham DH1 3LE, United Kingdom*
[3]*Department of Mechanical and Process Engineering, ETH Zurich, CH-8092 Zurich, Switzerland*

(Received 14 April 2019; published 24 July 2019)

We extend a recently proposed ternary free-energy lattice Boltzmann model with high density contrast [Phys. Rev. Lett. **120**, 234501 (2018)] by incorporating wetting boundaries at solid walls. The approaches are based on forcing and geometric schemes, with implementations optimized for ternary (and, more generally, higher-order multicomponent) models. Advantages and disadvantages of each method are addressed by performing both static and dynamic tests, including the capillary filling dynamics of a liquid displacing the gas phase and the self-propelled motion of a train of drops. Furthermore, we measure dynamic angles and show that the slip length critically depends on the equilibrium value of the contact angles and whether it belongs to liquid-liquid or liquid-gas interfaces. These results validate the model capabilities of simulating complex ternary fluid dynamic problems near solid boundaries, for example, drop impact solid substrates covered by a lubricant layer.

DOI: 10.1103/PhysRevE.100.013308

I. INTRODUCTION

Understanding the flow properties of ternary fluid systems is key in many natural phenomena and technological applications. In microfluidics, combinations of immiscible liquids are employed to produce multiple emulsions [1]. In food sciences and pharmacology, collisions between immiscible drops [2] and liquid streams [3] can be exploited to encapsulate liquids. Collisions are also particularly relevant in combustion engines, where encapsulation of water drops by fuel can induce microexplosions enhancing the burning rate [4]. Furthermore, in advanced oil recovery, the water-alternate-gas (WAG) techniques are frequently employed to enhance the recovery [5]. The oil-water interaction in dynamic conditions also poses environmental challenges. For example, the spilling of an oil layer at the surface of sea water strongly affects the production of marine aerosol when rain drops impact on the oil layer [6]. In contrast, placing a lubricant layer on a rough solid is the key idea behind the recent development of slippery lubricant impregnated surfaces (SLIPS), allowing us to virtually eliminate contact line pinning [7,8], with applications in coatings and packaging.

Several numerical schemes have been proposed in recent years to simulate ternary and higher-order fluid systems, including immersed boundary [9], level-set [10], and phase-field methods [11–15]. In this work we employ the lattice Boltzmann (LB) method [16,17]. Multiphase and multicomponent LB models are characterized by a diffuse interface, which has the advantage that the interface does not need to be tracked explicitly [18,19]. This makes diffuse interface models particularly convenient to study problems involving coalescence or break-up of liquids [20,21], drop collisions [22–25], drop impact on solid walls [26–31], and on topographic or chemically patterned surfaces [32,33].

Several LB models have been proposed to study ternary fluid systems. Travasso *et al.* proposed a free-energy model to study phase separation of ternary mixtures under shear [34]; Spencer *et al.* proposed a color model to study $N > 2$ component systems [35]; Ridl *et al.* proposed a model combining N Van der Waals equation of states to study the stability of multicomponent mixtures [36]; Semprebon *et al.* proposed a ternary free-energy approach [37] to model liquids with equal density, showing that the method can simulate drop morphologies on SLIPS [38] and their dynamic properties [39] for a wide range of surface tensions and contact angles.

To model effects of inertia, the large density ratio between liquids and the gas phase needs to be accounted [40,41], but only recently ternary models for high density ratio have been proposed. Shi *et al.* [42] extended the binary Cahn-Hilliard model for high density ratio proposed by Want *et al.* [43] to three components. Wöhrwag *et al.* proposed a free-energy functional combining multiphase and multicomponent terms [44], and employing the entropic collision approach [45] could simulate density contrast up to 10^3. The model could capture the salient features of head-on collisions between immiscible drops, reproducing the bouncing, adhesion, and encapsulation mechanisms previously observed experimentally [2].

In this work we extend this high-density ternary approach to model wetting of solid boundaries. The paper is organized as follows: In Sec. II we summarize the ternary model introduced in Ref. [44]. In Sec. III we perform an extensive analysis of the interfacial properties as function of the free-energy parameters. In Sec. IV we describe our implementation of three methods for wetting of solid boundaries, namely *force*, *geometric extrapolation*, and *geometric interpolation*, and benchmark the accuracy of contact angles in mechanical

*karlin@lav.mavt.ethz.ch
†halim.kusumaatmaja@durham.ac.uk
‡ciro.semprebon@northumbria.ac.uk

equilibrium. In Sec. V we compare the accuracy of the *force* and *geometric interpolation* methods in simulating the capillary filling of a two-dimensional (2D) channel. In Sec. VI we perform a ternary-specific benchmark, simulating a self-propelled bislug. This will enable us to evaluate the slip properties of the three fluid interfaces and assess the impact of different slip mechanisms. Finally, in Sec. VII, we summarize and discuss our results.

II. LATTICE BOLTZMANN FORMULATION

In this section, we summarize the derivation of the multiphase-multicomponent lattice Boltzmann model proposed in Ref. [44].

A. Ternary multiphase-multicomponent free energy

The ternary free-energy model is conveniently expressed in terms of a combination of bulk f_{Bulk} and the interfacial terms f_{Inter} in the free-energy functional:

$$F = \int [f_{\text{Bulk}} + f_{\text{Inter}}] dV, \tag{1}$$

where

$$f_{\text{Bulk}} = \frac{\lambda_1}{2}[\Psi_{\text{eos}}(\rho) - \Psi_0] + \frac{\lambda_2}{2} C_2^2 (1 - C_2)^2 + \frac{\lambda_3}{2} C_3^2 (1 - C_3)^2, \tag{2}$$

$$f_{\text{Inter}} = \frac{\kappa_1}{2}(\nabla\rho)^2 + \frac{\kappa_2}{2}(\nabla C_2)^2 + \frac{\kappa_3}{2}(\nabla C_3)^2. \tag{3}$$

The first term in Eq. (2) tunes the coexistence of high-density (ρ_l) liquid with a low-density (ρ_g) gas. The term $\Psi_{\text{eos}}(\rho)$ is derived by integrating any suitable nonideal equation of state, $p_{\text{eos}} = \rho(d\Psi_{\text{eos}}/d\rho) - \Psi_{\text{eos}}$. In our previous work [44] we have shown that the model can host various equations of state [46], including van der Waals, Peng-Robinson, and Carnahan-Starling. Here we employ the Carnahan-Starling equation of state:

$$\Psi_{\text{eos}} = \rho\left[C - a\rho - \frac{8RT(-6 + b\rho)}{(-4 + b\rho)^2} + RT\log(\rho)\right], \tag{4}$$

where the constants C and Ψ_0 enforce $\Psi_{\text{eos}}(\rho_g) = \Psi_{\text{eos}}(\rho_l) = \Psi_0$. This condition ensures that the common tangent construction is valid for all coexisting phases. Unless otherwise stated, we employ the following values $a = 0.037$, $b = 0.2$, and $R = 1$, for which the critical temperature is $T_c = 0.3373\frac{a}{bR}$. The critical temperature describes the temperature below which coexistence between the two liquids and the gas is possible and above which the liquid and gas phases are indistinguishable. The reduced temperature $T_r = T/T_c$ is employed to set the density contrast between the gas and the liquid phases, as shown in the coexistence curve reported in Ref. [44]. We define the relative concentration of the gas phase as

$$C_1 = \frac{\rho - \rho_l}{\rho_g - \rho_l}, \tag{5}$$

for which $C_1 = 0$ when $\rho = \rho_l$ and $C_1 = 1$ when $\rho = \rho_g$.

The second and third terms in Eq. (2) represent a double-well potential, as function of the relative liquid concentrations: C_2 and C_3. Each concentration has two minima at $C_{2,3} = 0$ and $C_{2,3} = 1$, corresponding to the presence or absence of the liquid. For convenience we introduce the phase field $\phi = \chi(C_2 - C_3)$ which, together with the density ρ, describes the system state. The parameter χ usually takes the value $\chi = 5$ in our model, and is employed to rescale the field ϕ such as the distance between minima is similar in both the ρ and ϕ fields. The variable transformations

$$C_2 = \frac{1}{2}\left[1 + \frac{\phi}{\chi} - \frac{\rho - \rho_l}{\rho_g - \rho_l}\right] \tag{6}$$

and

$$C_3 = \frac{1}{2}\left[1 - \frac{\phi}{\chi} - \frac{\rho - \rho_l}{\rho_g - \rho_l}\right], \tag{7}$$

enforce the constraint

$$C_1 + C_2 + C_3 = 1 \tag{8}$$

and allow us to map the density and phase fields to the concentration fields.

The bulk free-energy density in Eq. (2) describes three distinct energy minima in the (ρ, ϕ) space, corresponding to $(\rho, \phi) = (\rho_g, 0)$ (gas phase) and $(\rho_l, +\chi)$, $(\rho_l, -\chi)$ (liquid phases). The set of lambdas (λ_1, λ_2, and λ_3) tunes the magnitude of the energy barriers between each pair of phases.

Equation (3) contains gradient terms of the density field and the concentration of the two liquid components, describing the energy penalty in the formation of the interfaces, tuned by the set of kappas (κ_1, κ_2, and κ_3). Summarizing, this free-energy model depends on six independent parameters to fully determine the thermodynamic properties of the system.

B. Derivation of the pressure tensor

The chemical potentials μ_ρ and μ_ϕ are obtained directly from the free energy

$$\mu_\rho(\mathbf{r}) = \frac{\delta F}{\delta\rho(\mathbf{r})} = \mu_\rho^{\text{Bulk}} + \mu_\rho^{\text{Inter}}, \tag{9}$$

$$\mu_\phi(\mathbf{r}) = \frac{\delta F}{\delta\phi(\mathbf{r})} = \mu_\phi^{\text{Bulk}} + \mu_\phi^{\text{Inter}}. \tag{10}$$

For convenience we express the chemical potentials in terms of the relative concentrations and, to simplify the notation, we define the auxiliary function $g(x) = x(x - 1/2)(x - 1)$:

$$\mu_\rho^{\text{Bulk}} = \frac{\lambda_1}{2}\frac{d\Psi_{\text{eos}}}{d\rho} - \frac{\lambda_2}{\Delta\rho}g(C_2) + \frac{\lambda_3}{\Delta\rho}g(C_3), \tag{11}$$

$$\mu_\phi^{\text{Bulk}} = \frac{\lambda_2}{\chi}g(C_2) - \frac{\lambda_3}{\chi}g(C_3), \tag{12}$$

$$\mu_\rho^{\text{Inter}} = -\kappa_{\rho\rho}\nabla^2\rho - \kappa_{\rho\phi}\nabla^2\phi, \tag{13}$$

$$\mu_\phi^{\text{Inter}} = -\kappa_{\rho\phi}\nabla^2\rho - \kappa_{\phi\phi}\nabla^2\phi. \tag{14}$$

In Eq. (11) $d\Psi_{\text{eos}}/d\rho$ is the first derivative by the density of the nonideal equation of state, and $\Delta\rho = \rho_l - \rho_g$. For the Carnahan-Starling equation of state (eos) the first derivative of Eq. (4) is

$$\frac{d\Psi_{\text{eos}}}{d\rho} = C - 2a\rho + RT(1 + \log\rho) + \frac{16RT(b\rho - 12)}{(-4 + b\rho)^3}. \tag{15}$$

Furthermore, in Eqs. (13) and (14) the mixing coefficients for the gradient terms are

$$\kappa_{\rho\rho} = \left[\kappa_1 + \frac{\kappa_2 + \kappa_3}{4(\rho_g - \rho_l)^2}\right], \tag{16}$$

$$\kappa_{\phi\phi} = \frac{\kappa_2 + \kappa_3}{4\chi^2}, \tag{17}$$

$$\kappa_{\rho\phi} = -\frac{\kappa_3 - \kappa_2}{4\chi(\rho_g - \rho_l)}. \tag{18}$$

The pressure tensor can be inferred from the relation $\nabla \cdot \mathbf{P} = \rho\nabla\mu_\rho + \phi\nabla\mu_\phi$ and takes the form

$$\begin{aligned} P_{\alpha\beta} &= p_0\delta_{\alpha\beta} \\ &+ \kappa_{\rho\rho}\left\{(\partial_\alpha\rho)(\partial_\beta\rho) - \left[\rho(\partial_{\gamma\gamma}\rho) + \frac{1}{2}(\partial_\gamma\rho)^2\right]\delta_{\alpha\beta}\right\} \\ &+ \kappa_{\phi\phi}\left\{(\partial_\alpha\phi)(\partial_\beta\phi) - \left[\phi(\partial_{\gamma\gamma}\phi) + \frac{1}{2}(\partial_\gamma\phi)^2\right]\delta_{\alpha\beta}\right\} \\ &+ \kappa_{\rho\phi}\{(\partial_\alpha\rho)(\partial_\beta\phi) + (\partial_\alpha\phi)(\partial_\beta\rho) \\ &- [\rho(\partial_{\gamma\gamma}\phi) + \phi(\partial_{\gamma\gamma}\rho) + (\partial_\gamma\rho)(\partial_\gamma\phi)]\delta_{\alpha\beta}\}, \end{aligned} \tag{19}$$

where p_0 is the pressure in the fluid bulk

$$p_0 = \rho\mu_\rho^{\text{Bulk}} + \phi\mu_\phi^{\text{Bulk}} - f_{\text{Bulk}}. \tag{20}$$

C. Entropic lattice Boltzmann implementation

The dynamic evolution of the isothermal ternary system follows the continuity, Navier-Stokes, and Cahn-Hilliard equations:

$$\partial_t\rho + \nabla\cdot(\rho\mathbf{v}) = 0, \tag{21}$$

$$\partial_t(\rho\mathbf{v}) + \nabla\cdot(\rho\mathbf{v}\otimes\mathbf{v}) = -\nabla\cdot\mathbf{P} + \nabla\cdot[\eta(\nabla\mathbf{v} + \nabla\mathbf{v}^{\mathbf{T}})], \tag{22}$$

$$\partial_t\phi + \nabla\cdot(\phi\mathbf{v}) = M\nabla^2\mu_\phi, \tag{23}$$

where $\mathbf{v}$ is the fluid velocity, η is the dynamic viscosity, and M represents the mobility in the Cahn-Hilliard model for the order parameter ϕ.

To solve the equations of motion we introduce two sets of distribution functions, evolving the density ρ and the order parameter ϕ. For the density ρ, we employ the entropic lattice Boltzmann method (ELBM) [40,47], as it provides an enhanced numerical stability when there is a large density ratio between the liquid and gas phases,

$$\begin{aligned} &f_i(\mathbf{x} + \mathbf{c}_i\Delta t, t + \Delta t) \\ &\quad = f_i(\mathbf{x}, t) + \alpha\beta\left[f_i^{\text{eq}}(\rho, \mathbf{u}) - f_i(\mathbf{x}, t)\right] + F_i. \end{aligned} \tag{24}$$

We implement the exact form for the equilibrium distribution function $f_i^{\text{eq}}(\rho, \mathbf{u})$, which for a D-dimensional system (described by the lattices D1Q3, D2Q9, or D3Q27) can be written in the product form [48,49],

$$f_i^{\text{eq}} = \rho w_i \Pi_{\alpha=1}^{D} A(u_\alpha)[B(u_\alpha)]^{c_{i\alpha}}. \tag{25}$$

The w_i's are the lattice weights and $c_{i\alpha}$ is the α component of the $\mathbf{c}_i$th lattice vector. The functions $A(u)$ and $B(u)$ are given by

$$A(u) = 2 - \sqrt{1 + 3u^2} \tag{26}$$

and

$$B(u) = \frac{2u + \sqrt{1 + 3u^2}}{1 - u}. \tag{27}$$

The forcing term F_i in Eq. (24) [23] is implemented via the exact differences scheme

$$F_i = \left[f_i^{\text{eq}}(\rho, \mathbf{u} + \delta\mathbf{u}) - f_i^{\text{eq}}(\rho, \mathbf{u})\right], \tag{28}$$

where $\rho\mathbf{u} = \sum_i f_i\mathbf{c}_i = \sum_i f_i^{\text{eq}}\mathbf{c}_i$ is the bare fluid velocity and $\delta\mathbf{u} = (\mathbf{F}/\rho)\Delta t$ is the correction to the fluid velocity arising from the force

$$\mathbf{F} = \nabla\cdot\left(\rho c_s^2\mathbf{I} - \mathbf{P}\right). \tag{29}$$

In Eq. (29) $c_s^2 = 1/3$ is the speed of sound in the lattice Boltzmann scheme.

In ELBM the parameter β tunes the kinematic viscosity $\nu = \eta/\rho = (\beta^{-1} - 1)/6$, and the parameter α is the nontrivial root of

$$H(f' + \alpha[f^{\text{eq}}(\rho, \mathbf{u} + \delta\mathbf{u}) - f']) = H(f'). \tag{30}$$

In Eq. (30)

$$f_i' = f_i + \left[f_i^{\text{eq}}(\rho, \mathbf{u} + \delta\mathbf{u}) - f_i^{\text{eq}}(\rho, \mathbf{u})\right] \tag{31}$$

represents the mirror state, and

$$H(f) = \sum_i f_i \ln(f_i/w_i) \tag{32}$$

is the entropy.

To evolve the order parameter ϕ, we employ a standard lattice Bhatnagar-Gross-Krook (LBGK) scheme

$$g_i(\mathbf{x} + \mathbf{c}_i\Delta t, t + \Delta t) = g_i(\mathbf{x}, t) + \frac{\left[g_i^{\text{eq}}(\phi, \mathbf{v}) - g_i(\mathbf{x}, t)\right]}{\tau}. \tag{33}$$

The parameter τ is related to the mobility $M = \Gamma(\tau - 1/2)$ in Eq. (23), where the constant Γ tunes the diffusivity and is chosen to be $\Gamma = 1$ unless otherwise stated. The equilibrium distribution function, $g_i^{\text{eq}}(\phi, \mathbf{v})$, can be written as

$$\begin{aligned} g_i^{\text{eq}}(\phi, \mathbf{v}) = w_i\Bigg[&\frac{\Gamma\mu_\phi}{c_s^2} + \frac{\phi v_\alpha c_{i\alpha}}{c_s^2} \\ &+ \frac{\phi v_\alpha v_\beta\left(c_{i\alpha}c_{i\beta} - c_s^2\delta_{\alpha\beta}\right)}{2c_s^4}\Bigg], \end{aligned} \tag{34}$$

$$g_0^{\text{eq}}(\phi, \mathbf{v}) = \phi - \sum_{i\neq 0} g_i^{\text{eq}}, \tag{35}$$

where the actual fluid velocity, $\mathbf{v} = \mathbf{u} + \delta\mathbf{u}/2$, is required.

III. SURFACE TENSIONS

In free-energy models based on double-well potentials [50,51], the shape of the concentration profile against the spatial coordinates takes the form of a hyperbolic tangent. This feature is inherited in our ternary model but only for the liquid-liquid interface between phases C_2 and C_3, which is characterized by the parameter

$$\alpha_{23} = \sqrt{\frac{\kappa_2 + \kappa_3}{\lambda_2 + \lambda_3}}. \tag{36}$$

TABLE I. Parameters of four selected sets and the relative surface tensions and Neumann angles. The last row reports the global energy minimum configuration of a double emulsion. The white region corresponds to the gas phase (C_1), while the blue and red regions correspond to the liquids C_2 and C_3.

Set	**1**	**2**	**3**	**4**
λ_1	0.6	0.6	0.01	0.1
κ_1	0.01	0.01	0.01	0.01
λ_2	1.0	1.1	1.5	1.0
κ_2	1.0	1.1	1.5	1.6
λ_3	1.0	0.5	1.5	0.2
κ_3	1.0	0.5	1.5	−0.4
γ_{12}	0.414	0.431	0.333	0.321
γ_{13}	0.414	0.334	0.333	0.120
γ_{23}	0.323	0.259	0.485	0.180
θ_1	134.1	143.1	86.3	—
θ_2	112.9	129.2	136.8	—
θ_3	112.9	87.6	136.8	—
			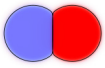	

We can assume that the density does not vary at the interface between C_2 and C_3 and set $C_1 = 0$ along the interface. Following Ref. [37], if the coordinate x measures the distance from the interface along its normal direction, then the concentration profiles of the components C_2 and C_3 vary according to

$$C_{2,3}(x) = \frac{1 \pm \tanh \frac{x}{2\alpha_{23}}}{2}. \tag{37}$$

Integrating of the concentration profiles along x we derive a simple expression for the surface tension [37],

$$\gamma_{23} = \frac{\alpha_{23}}{6}(\lambda_2 + \lambda_3). \tag{38}$$

For the liquid-gas interfaces, it is not possible to assume *a priori* that the ρ and ϕ fields vary with the same functional form. Indeed, the minimization of the free energy seeks a path which cannot be described analytically. To illustrate this aspect, we study in detail four cases, represented by the parameter sets reported in Table I. For each set we independently compute for all interfaces the surface tension $\gamma = \Delta P R$ by measuring the pressure jump ΔP across the interface of 2D drop of radius R (bubble test).

The four sets are listed in order of increasing mismatch between the interfacial profiles. The first set represents two liquids with symmetric properties, where the liquid-liquid surface tension is slightly lower than both the liquid-gas ones. The second set describes three fluids with different properties. The third set also describes two equal liquids but λ_1 is much smaller than in the first set, leading to a liquid-liquid surface tension significantly larger than the liquid-gas ones. The fourth set describes also three fluids, but in this case the parameter κ_3 is negative, leading to a spontaneous encapsulation of liquid C_2 by liquid C_3. Negative values of lambdas or kappas are generally allowed in the ternary model, as long as the three minima in the $[\rho, \phi]$ space are well defined.

In Fig. 1 we inspect the properties of the diffuse interfaces for the parameter sets described in Table I. The color maps illustrate the contours of the bulk free energy in the $[\phi, \rho]$ space. As expected, the bulk free energy is symmetric in ϕ for sets 1 and 3 and nonsymmetric for sets 2 and 4.

Introducing the variable transformation Eqs. (5), (6), and (7) into Eq. (8) we can easily see that the absence of the third component at any interface leads to a linear relation between ρ and ϕ connecting the corresponding minima, represented by straight lines in the $[\rho, \phi]$ space in Fig. 1. However, the minimization of the free energy does lead to different paths, depicted by connected dots. As Eq. (8) must be satisfied, the inverse variable transformation will produce a certain fraction of the minor component at the interface.

For set 1, the paths in the $[\phi, \rho]$ space are close to straight lines. The deviations in the remaining sets increase with the increasing mismatch between the profiles of ρ and ϕ. To quantify these mismatches we define the "concentration deviation coefficient" D as the difference between the maximum and minimum values of the minority phase in a region Ω near the interface between the two majority phases. Figure 2 illustrates a typical example of the spatial variation of the minority concentration C_3 at the interface between C_1 and C_2. The concentration deviation coefficient D_3 is then defined as

$$D_3 = \max_{\mathbf{x}\in\Omega}(C_3) - \min_{\mathbf{x}\in\Omega}(C_3) \tag{39}$$

and similarly for the other interfaces. For an ideal system, D_1, D_2, $D_3 \to 0$.

In our model the surface tensions cannot be computed analytically. Thus, we have performed a systematic investigation into how the liquid-liquid and liquid-gas surface tensions depend on the six-dimensional parameter space formed by $\boldsymbol{\lambda} = (\lambda_1, \lambda_2, \lambda_3)$ and $\boldsymbol{\kappa} = (\kappa_1, \kappa_2, \kappa_3)$. However, since exploring the full six-dimensional parameter space is too demanding, here we have identified eight relevant subspaces. In all cases, we set $T_{\text{red}} = 0.61$, which leads to an effective density ratio $\rho_l/\rho_g \simeq 10^3$.

Each subspace is described by two coordinates, X and Y, and it is mapped using a $20 \times 20 = 400$ points grid, where each point represents a given parameter set. For each point, we have performed three independent drop (or bubble) tests in order to measure the surface tensions of the three fluid-fluid interfaces. The spatial variations of the concentrations are also measured along the radial direction from the center of the drop (or bubble) to the boundary of the simulation domain. This allows us to characterize the concentration deviation coefficient for the minority phase, as defined in Eq. (39).

The maps $\boldsymbol{\lambda}(X, Y)$ and $\boldsymbol{\kappa}(X, Y)$ are summarized in Table II. In Subspace 1 we consider immiscible liquids with identical properties $\lambda_2 = \lambda_3 = \kappa_2 = \kappa_3 = X$ and explore the relative effect of the variation in the liquid-gas contribution to the bulk free energy $\lambda_1 = Y$. Subspace 2 is similar, but the choice of $\lambda_2 = \lambda_3 = \kappa_2 = \kappa_3$ produces a larger width of liquid-liquid interface, resulting in lower Neumann angles for the gas phase θ_1 (more repelling liquids). In Subspace 3 we fix $\lambda_3 = \kappa_3 = 0.5$, and explore the interplay between the gas phase and the first liquid. This set is useful to simulate system with nonsymmetric interfacial properties for the two liquids. In

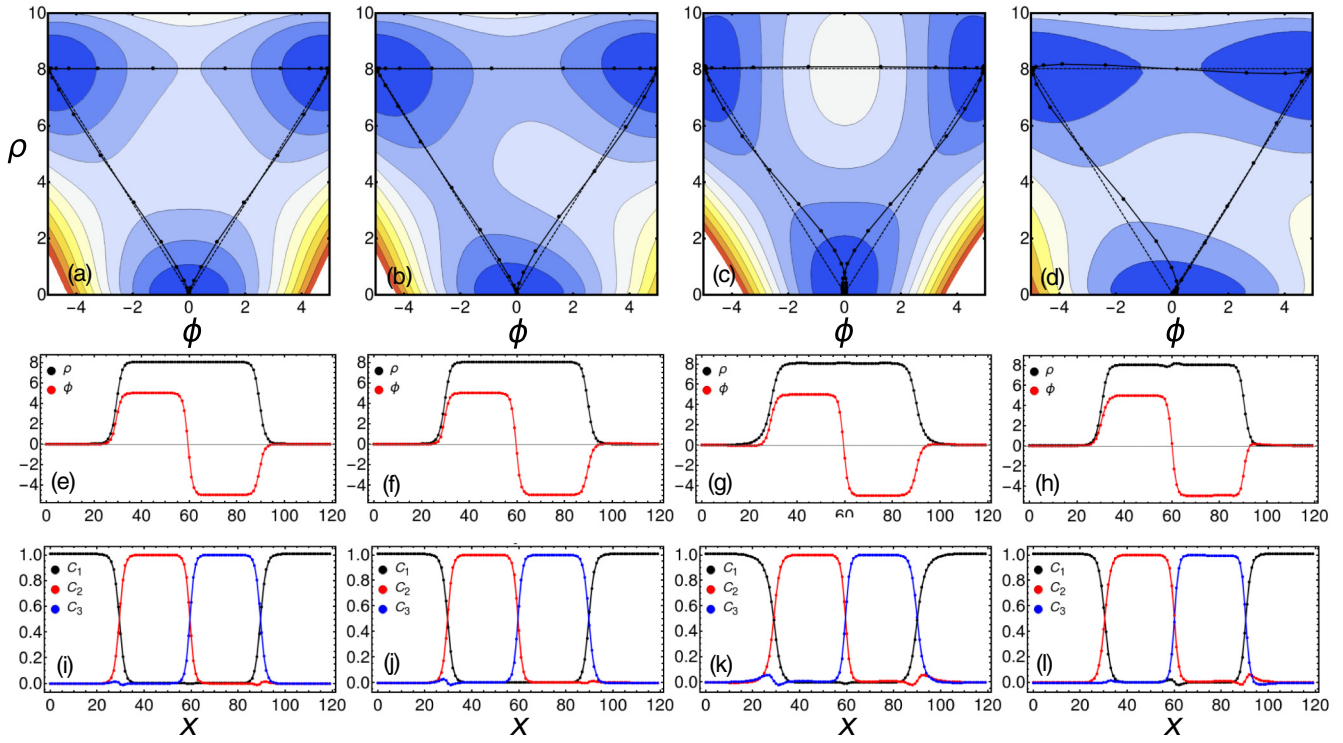

FIG. 1. Upper row: Color maps of the bulk free energy for the parameter sets 1, 2, 3, and 4 [panels (a), (b), (c), and (d)]. The dashed lines connecting the three energy minima represent the path in the of $[\phi, \rho]$ space of an ideal interface, where the third components is completely absent. Data points represent the path of the numerically computed interface profiles in mechanical equilibrium. Deviations from the dashed lines reveal the creation of a fraction of concentration the third component. Middle row [panels (e), (f), (g), and (h)]: Profiles of ρ and ϕ along interfaces between fluids, placed in the sequence 1,2,3,1. Bottom row [panels (i), (j), (k), and (l)]: Profiles of C_1, C_2, and C_3 along interfaces between fluids in the corresponding sequence 1,2,3,1.

Subspaces 4, 5, and 6 we fix the the contributions of the bulk term for the equation of state to three values, $\lambda_1 = 0.01, 0.6, 1.0$. These lead respectively to a small, medium, and large contribution to the liquid-gas surface tensions from the bulk term. In all three subspaces we then systematically explore parameter combinations for the two liquids $\lambda_2 = \kappa_2 = X$ and $\lambda_3 = \kappa_3 = Y$, allowing us to realize systems with enhanced asymmetry in the surface tension properties of the liquids. In Subspaces 7 and 8 we consider cases with negative values of κ_2, which are necessary to achieve spontaneous encapsulation of liquid 3 by liquid 2. The parameters can be tuned in order to compare systems where the spreading parameters S_2 continuously shifts from positive to negative.

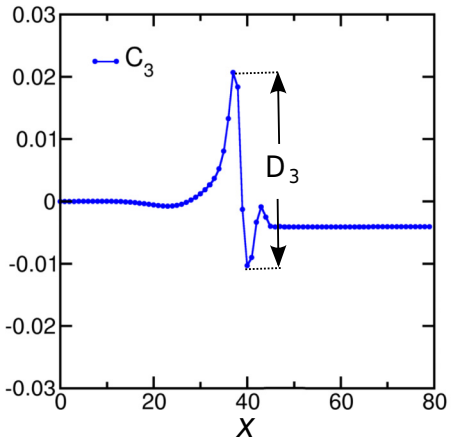

FIG. 2. Example of profile of the concentration C_3 at the interface between C_1 and C_2 illustrating the definition of the concentration deviation coefficient (D_3).

In Fig. 3 we report, as an example, our analysis of the subspace 4. The first row of panels depicts the surface tensions γ_{12}, γ_{13}, and γ_{23}, respectively. As expected, γ_{12} and γ_{13} mainly depend on the variation of $X = \lambda_2$ and $Y = \lambda_3$, respectively, while γ_{23} is function of $X + Y = \lambda_2 + \lambda_3$. The nonperfect alignment of the contour lines with the main axes for γ_{12} and γ_{13} is an indication of the nonconstant contribution of the liquid-gas component, even if λ_1 is fixed throughout the subspace. The variation of γ_{23} instead is more regular, because

TABLE II. Summary of surface tension tests. Details for each case are in the Supplemental Material [52].

Subspace	λ_1	λ_2	λ_3	κ_1	κ_2	κ_3
1	Y	X	X	0.01	X	X
2	Y	X	X	0.01	$0.5X$	$0.5X$
3	Y	X	0.5	0.01	X	0.5
4	0.01	X	Y	0.01	X	Y
5	0.5	X	Y	0.01	X	Y
6	1.0	X	Y	0.01	X	Y
7	Y	X	0.5	0.01	$2X - 0.5$	$1 - X$
8	0.1	X	1.0	0.01	Y	$1 + X - Y$

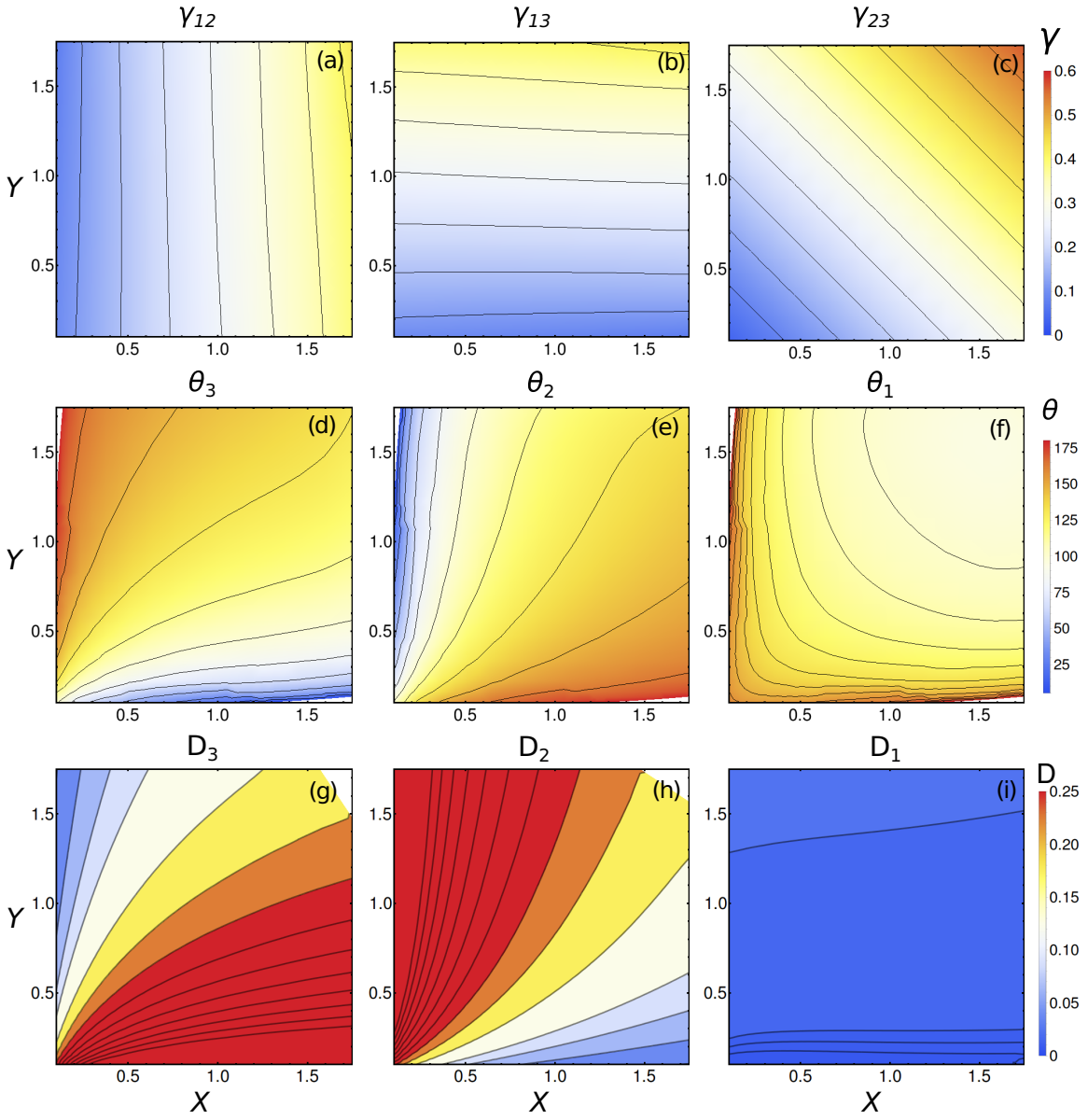

FIG. 3. Color maps of relevant quantities as function of the coordinate $X = \lambda_2$ and $X = \lambda_3$. Upper row [(a), (b), and (c)]: surface tensions (λ_{12}, λ_{13}, and λ_{23}); middle row [(d), (e), and (f)]: Neumann angles (θ_3, θ_2 and θ_1); Lower row [(g), (h), and (i)]: concentration deviation coefficient (D_3, D_2, and D_1).

no variation of the density field occurs at this interface and closely follows the values of surface tension predicted by Eq. (38) (comparison not shown).

The second row of panels in Fig. 3 reports the Neumann angles θ_1, θ_2, and θ_3 computed as functions of the surface tensions:

$$\cos\theta_1 = \frac{\gamma_{23}^2 - \gamma_{12}^2 - \gamma_{13}^2}{2\gamma_{12}\gamma_{13}}, \tag{40}$$

$$\cos\theta_2 = \frac{\gamma_{13}^2 - \gamma_{12}^2 - \gamma_{23}^2}{2\gamma_{12}\gamma_{23}}, \tag{41}$$

$$\cos\theta_3 = \frac{\gamma_{12}^2 - \gamma_{13}^2 - \gamma_{23}^2}{2\gamma_{13}\gamma_{23}}. \tag{42}$$

For the full range of parameters explored in this subspace, the Neumann angles are always well defined, indicating that the spreading parameter $S_k = \gamma_{ij} - \gamma_{ik} - \gamma_{jk} < 0$. The third row of panels in Fig. 3 reports the "concentration deviation coefficient" D, measured for each interface. As expected, $D_1 \simeq 0$ throughout the whole map. In contrast, D_2 and D_3 vary up to 25% of the concentration interval ([0,1]).

Similar analysis to Fig. 3 for all other subspaces in Table II are provided in the Supplemental Material [52]. We have also fitted the maps of surface tension with a two-variable polynomial function.

$$\gamma = A(X) + B(X)Y + C(X)Y^2, \tag{43}$$
$$A(X) = a_1 + a_2 x + a_3 x^2 + \ldots,$$
$$B(X) = b_1 + b_2 x + b_3 x^2 + \ldots,$$
$$C(X) = c_1 + c_2 x + c_3 x^2 + \ldots.$$

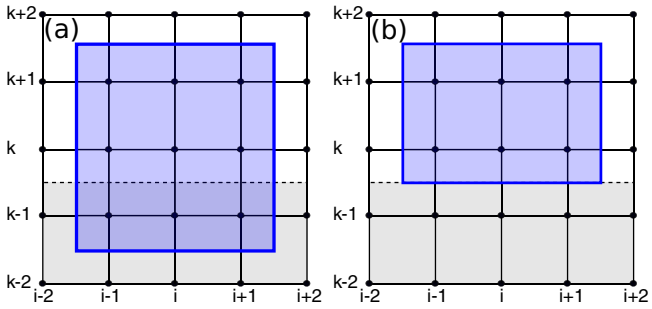

FIG. 4. Sketch in 2D of the stencils employed for the computation of gradients. (a) The stencil for $\nabla\rho$, $\nabla\phi$, $\nabla^2\rho$, and $\nabla^2\phi$ is the same as in the fluid bulk and relies on the quantities stored in the ghost nodes in the solid layer. (b) The stencil for $\nabla\mathbf{P}_\parallel$ excludes solid nodes, where $\mathbf{P}$ is not defined.

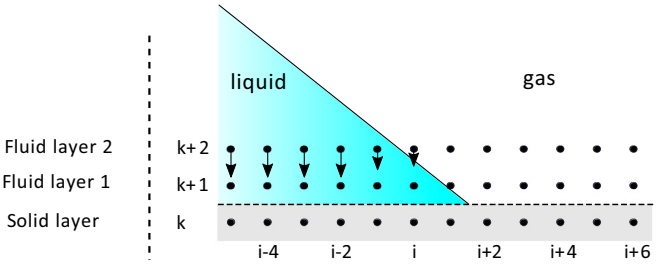

FIG. 5. Sketch of the forcing terms acting near the liquid-liquid interface in contact to a solid boundary. The arrows represent the direction and magnitude of the local force Eq. (44).

The values of the a_i, b_i, and c_i coefficients for the three fluid-fluid interfaces are tabulated in the Supplemental Material [52]. Thus, the database can be used to choose the target combinations of surface tensions and correspondingly the free-energy parameters in our model. Typically, to choose the parameter sets for our simulations, we perform the following steps:

(1) Identify a suitable subset out of the eight presented here, considering (i) whether the two liquid-gas surface tensions are the same or different, (ii) whether the liquid-liquid surface tension should be larger or smaller than the liquid-gas tensions, and (iii) whether a positive spreading parameter (for spontaneous encapsulation to occur) is required.

(2) Each subset is described in terms of two coordinates X and Y, as summarized in Table II. Identify the values of X and Y that match the required surface tension properties. The fitting functions provided in the Supplemental Material [52] for each subset map the free-energy parameters (in terms of the coordinates X and Y) to the liquid-liquid and liquid-gas surface tensions. A compromise may be needed to minimize the concentration deviation coefficient as defined in Eq. (39).

IV. SOLID BOUNDARIES

In this section we describe and benchmark our implementation of solid boundaries. For simplicity we consider only flat walls, aligned with the domain axis and located at half distance between lattice nodes, but all methods can be easily extended to solid structures with corners and wedges.

In all methods we treat the first layer of solid nodes as ghost nodes to store values of ρ and ϕ. These values are employed in the finite-difference stencils to compute $\nabla\rho$, $\nabla\phi$, $\nabla^2\rho$, and $\nabla^2\phi$ in order to evaluate the chemical potentials and the pressure tensor [Eqs. (13), (14), and (19)] of the fluid near the solid boundaries, as illustrated in Fig. 4(a).

Throughout the whole fluid domain, the forces are computed by numerically differentiating the pressure tensor in Eq. (29). As $\mathbf{P}$ is not defined on the solid nodes, its partial derivatives in the first fluid layer are computed differently. Specifically, near the solid boundaries we impose $\nabla\mathbf{P}_\perp = 0$ (perpendicular to the solid), while a one-sided biased gradient [27] is employed for the gradient $\nabla\mathbf{P}_\parallel$ (parallel to the solid), as illustrated in Fig. 4(a). After the collision and streaming steps, standard bounce-back rules are applied [53].

A. Method 1 (force)

The forcing method [47,54] is inspired by pseudopotential models for multicomponent fluids, where the liquid-solid interaction is introduced through a forcing term. In our implementation, the values of ρ and ϕ in the ghost nodes at the solid layer are constantly updated by copying the values in the first fluid layer. This procedure alone gives to the solid neutral wetting properties. In this method, higher or lower affinity of the fluid phases to the solid are obtained by adding a local force term:

$$\mathbf{F}_s(\mathbf{x},t) = \rho^{\mathrm{rel}}(\mathbf{x})\left[\kappa_\rho^w + \phi^{\mathrm{rel}}(\mathbf{x})\kappa_\phi^w\right]\sum_i w_i s(\mathbf{x}+\mathbf{c}_i\delta t)\mathbf{c}_i, \tag{44}$$

where s is a function that takes a value of 1 on fluid nodes connected two lattice vectors away from solid nodes. In practice, for a flat substrate as in the sketch in Fig. 5, s takes value 1 on the second layer of fluid nodes only. We apply the force to the second fluid layer instead of the first one (as proposed in other works [47]) to improve the stability of the algorithm. One can easily verify that force terms of smaller magnitude are necessary at the second fluid layer to obtain the same target contact angle.

The prefactor $\rho^{\mathrm{rel}}(\mathbf{x})[\kappa_\rho^w + \phi^{\mathrm{rel}}(\mathbf{x})\kappa_\phi^w]$ accounts for the variation of the interaction strength as function of the fields ρ and ϕ, tuned by the parameters κ_ρ^w and κ_ϕ^w. We employ the rescaled fields $\rho^{\mathrm{rel}}(\mathbf{x}) = [\rho(\mathbf{x}) - \rho_g]/(\rho_l - \rho_g)$ and $\phi^{\mathrm{rel}}(\mathbf{x}) = \phi(\mathbf{x})/\chi$, which vary in the interval [0,1] and [−1.1], respectively.

Furthermore, for the stability of the algorithm it is essential that no large forcing terms are applied in the gas phase ($[\rho,\phi] = [\rho_g, 0]$), which is achieved by multiplying both κ_ρ^w and κ_ϕ^w by $\rho^{\mathrm{rel}}(\mathbf{x})$ in our approach. In absence of this precaution, large forcing terms would cause strong deviations of the gas density from the equilibrium thermodynamic value.

When defining a contact angle between two phases we indicate with the first index the phase in which a contact angle is measured and with the second index the other phase. In our work we adopt the convention of measuring the angles in the liquid phase at liquid-gas interfaces, while at the liquid-liquid interface we measure the angle in the liquid with index 2. The

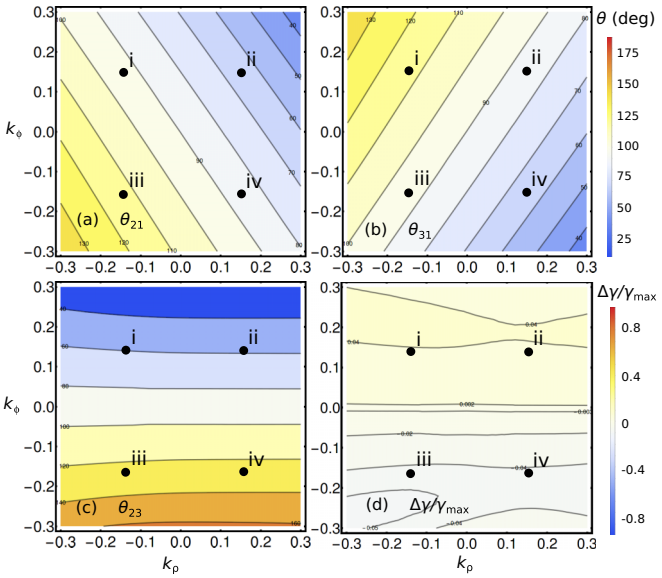

FIG. 6. Color maps of equilibrium contact angles measured from sessile drops, as functions of κ_ρ^w and κ_ϕ^w. Panels (a)–(c) refer to the interfaces [1,2], [1,3], and [2,3], respectively. Panel (d) reports the quantity $\Delta\gamma$ [Eq. (45)]. The combinations of surface tensions are given by the first set in Table I. The black dots labeled by letters (i)–(iv) refer the the double emulsions depicted in Fig. 7.

following relations are implied: $\theta_{12} = \pi - \theta_{21}, \theta_{13} = \pi - \theta_{31}$, and $\theta_{32} = \pi - \theta_{23}$.

A typical dependence of θ_{21}, θ_{31}, and θ_{23} from the parameters κ_ρ^w and κ_ϕ^w is reported in Figs. 6(a)–6(c) for the parameter set 1 in Table I. Contact angles are measured after equilibrating 2D sessile drops for each interface and fitting the drop interfaces with circular profiles. To keep the accuracy of the contact angle, across the whole parameter range, the drop area is fixed to $\simeq 100^2$ l.u.^{2} while the size and aspect ratio of the simulation domain is adjusted to accommodate drops of different shapes.

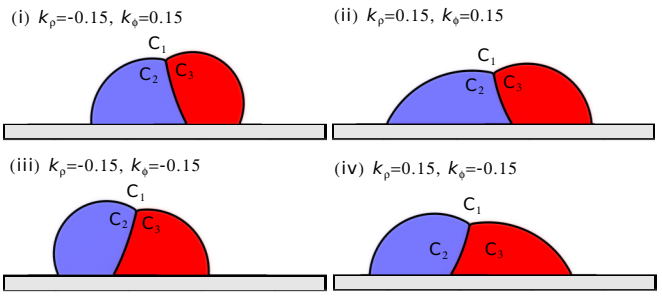

FIG. 7. Double emulsions in contact with a solid surface in mechanical equilibrium. The combination of surface tensions are given by the first set in Table I, while the wetting properties are introduced using the force method by setting: (i) $\kappa_\rho^w = -0.15$ and $\kappa_\phi^w = 0.15$, leading to $\theta_{21} = 94.35$, $\theta_{31} = 113.19$, and $\theta_{23} = 57.89$; (ii) $\kappa_\rho^w = 0.15$ and $\kappa_\phi^w = 0.15$, leading to $\theta_{21} = 64.96$, $\theta_{31} = 85.26$, and $\theta_{23} = 56.15$; (iii) $\kappa_\rho^w = -0.15$ and $\kappa_\phi^w = -0.15$, leading to $\theta_{21} = 113.19$, $\theta_{31} = 94.35$, and $\theta_{23} = 122.34$; and (iv) $\kappa_\rho^w = 0.15$ and $\kappa_\phi^w = -0.15$, leading to $\theta_{21} = 85.26$, $\theta_{31} = 64.96$, and $\theta_{23} = 124.15$.

The maps, as shown in Fig. 6, are specific for each set of free-energy parameters. For example, the inclination of the diagonal contour lines of θ_{21}, θ_{31} depends on the value of the surface tension for each interface. θ_{23} instead is predominantly a function of κ_ϕ^w, with only a residual dependence on κ_ρ^w in the region of small κ_ϕ^w.

On ideal surfaces the combinations of contact angles are not independent but obey the Girifalco-Good relation [55], which, according to our convention, reads

$$0 = \Delta\gamma = \gamma_{23}\cos\theta_{23} - \gamma_{13}\cos\theta_{31} + \gamma_{12}\cos\theta_{21}. \quad (45)$$

This condition is automatically satisfied by the force method, as can be deduced from Fig. 6(d), which reports the variation of $\Delta\gamma$ on a scale set by the largest value surface tension in the system ($\gamma_{\max} \simeq 0.5$). Small deviations identified by the contour lines can be attributed to the uncertainties in the measurement of the contact angles. The Girifalco-Good relation is a good test for benchmarking the thermodynamic consistency of wetting boundary conditions for ternary systems.

To further emphasize that our approach does translate to wetting phenomena involving ternary systems, we show four examples of double liquid emulsions in contact with a solid substrate, where the wetting properties are given by $\kappa_\rho^w = \pm 0.15$ and $\kappa_\phi^w = \pm 0.15$. We note that the contact angles measured in these double emulsion examples are essentially the same as the values measured when only binary systems are simulated (Fig. 6). The Good-Girifalco relation is also satisfied.

B. Methods 2 and 3 (geometric approaches)

We now introduce the two geometric approaches employed in our model. The key idea in both models is to manipulate the values of the fields in the ghost nodes at the solid boundaries according to a geometrical criterion in order to reproduce a prescribed contact angle. In both cases, the ternary implementation requires us to identify in advance the correct interface in order to select the correct target contact angle. This step is performed by implementing a set of rules that combine the local value of ρ and ϕ and of their gradients parallel to the solid $\nabla_\parallel\rho$ and $\nabla_\parallel\phi$:

$$\begin{cases} \text{if } |\nabla_\parallel\rho|/|\nabla_\parallel\phi| < 0.01(\rho_l - \rho_g)/\chi & \text{set interface 2-3} \\ \text{if } \nabla_\parallel\rho\cdot\nabla_\parallel\phi < 0 & \text{set interface 1-3} \\ \text{if } \nabla_\parallel\rho\cdot\nabla_\parallel\phi > 0 & \text{set interface 1-2}. \\ \text{if } \rho > \rho_l/2 \text{ and } \phi < -0.95\chi & \text{set interface 1-3} \\ \text{if } \rho > \rho_l/2 \text{ and } \phi > 0.95\chi & \text{set interface 1-2} \end{cases}$$

This set of rules proves to be accurate in all our tests, even if the variation of ρ and ϕ is not strictly monotonous near the interface. An alternative approach consists in weighting the contact angles based on the local concentration fields [13].

1. Geometric extrapolation

We now introduce our ternary implementation of the method proposed by Ding and Spelt [56]. The key idea is to compute the normal vector of a fluid interface in contact with the solid surface from the gradient of a field: $\mathbf{n}_s = \nabla c/|\nabla c|$. We employ $c = \rho$ at any liquid-gas interface and $c = \phi$ for the liquid-liquid interface. Referring to the sketch

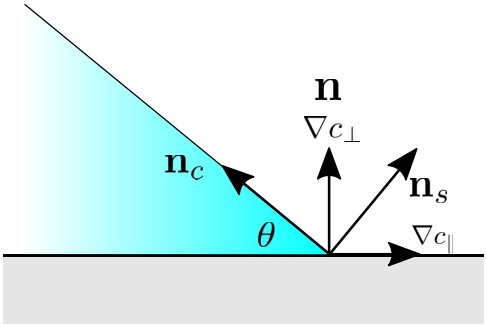

FIG. 8. Sketch of the main vectors defined by fluid interface near the contact line.

of the contact line geometry in Fig. 8, $\mathbf{n}$ defines the vector normal to a plane solid surface, while the perpendicular and parallel components of a field gradient can be expressed as $\nabla c_\perp = \mathbf{n}\cdot\nabla c$ and $\nabla c_\parallel = |\nabla c - (\mathbf{n}\cdot\nabla c)\mathbf{n}|$.

In the algorithm, first the parallel component of the gradient $\nabla c_\parallel$ is measured along the surface, and then it is employed to reconstruct the perpendicular component of the gradient $\nabla c_\perp$. For a diffuse interface forming an angle θ with the solid surface, the relation between components of the field gradients is given by

$$\nabla c_\perp = \tan\left(\frac{\pi}{2}-\theta\right)\nabla c_\parallel. \tag{46}$$

For example, in a 2D lattice addressed by the indices i, k, let us assume the layer k represents a solid surface for any i, while the layer $k+1$ represents the first fluid layer. The values of the field $c_{i,k}$ are computed by extrapolating the from the field value in the above layer

$$c_{i,k} = c_{i,k+1} + \nabla c_\perp, \tag{47}$$

where c represents either ρ or ϕ. For this reason, we denote this method as *geometric extrapolation*.

The 3D implementation differs from the 2D case only by replacing the component parallel to the surface of the concentration gradients with the norm of the two components in the plane. For example, if x and y define the coordinates in the plane, then we have $|\nabla_\parallel c| = \sqrt{(\nabla_x c)^2 + (\nabla_y c)^2}$ for a solid plane at $z = \text{const}$. The correction applies both in the determination of the interface and in the reconstruction of the perpendicular component $\nabla_\perp c$.

2. Geometric interpolation

This third method is inspired by the algorithm proposed by Lee and Kim [57]. Here the key idea is to interpolate the field values from the upper layer, where the interpolating point is shifted according to the slope of the liquid interface.

For a few special values of contact angles the slope of the interface connects to lattice nodes, and the required values of the field correspond exactly to the values already stored. Let us consider a 2D example: For the three nearest lattice nodes along the direction i of the solid surface we can simply assign

$$\begin{aligned} c_{i,k}|_{\theta\simeq 18.43^\circ} &= c_{i-3,k+1} \\ c_{i,k}|_{\theta\simeq 26.56^\circ} &= c_{i-2,k+1} \\ c_{i,k}|_{\theta=45^\circ} &= c_{i-1,k+1} \end{aligned}$$

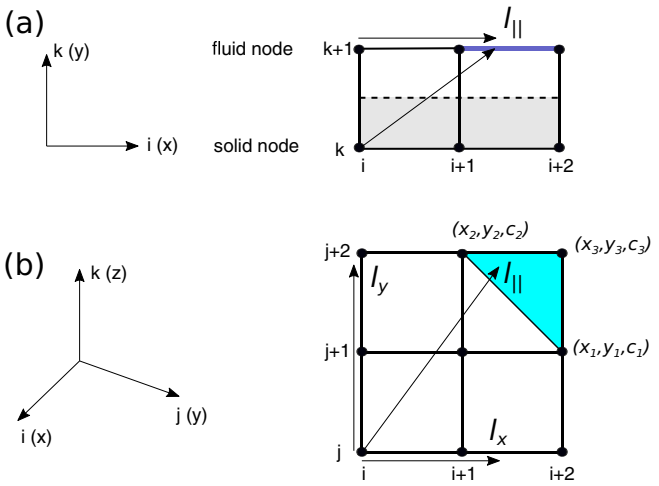

FIG. 9. Sketch of the *geometry interpolation* boundaries: (a) Two-dimensional implementation: The selected interval for the linear interpolation is highlighted. (b) Three-dimensional implementation: The selected triangle for the planar interpolation is highlighted.

$$\begin{aligned} c_{i,k}|_{\theta=90^\circ} &= c_{i,k+1} \\ c_{i,k}|_{\theta=45^\circ} &= c_{i+1,k+1} \\ c_{i,k}|_{\theta\simeq 153.43^\circ} &= c_{i+2,k+1} \\ c_{i,k}|_{\theta\simeq 161.56^\circ} &= c_{i+3,k+1}. \end{aligned} \tag{48}$$

For any other slope, instead we linearly interpolate the values of the two closest nodes. For this reason we denote this method as *geometric interpolation*. As shown in Fig. 9(a), in the 2D implementation we compute the distance of the interpolating point from the node i as $l_\parallel = \tan(\theta - \pi/2)$. In a local coordinate system centered in the node (i,k), the interpolating points are located at $l_0 = \text{floor}(l_\parallel)$ and $l_1 = \text{floor}(l_\parallel) + 1$, and their lattice indices are $i_0 = i + l_0$ and $i_1 = i + l_1$. Considering that $l_1 - l_0 = 1$, the linear interpolation scheme is

$$c_{i,k} = \left(c_{i_1,k+1} - c_{i_0,k+1}\right)l_\parallel + \left(l_1 c_{i_0,k+1} - l_0 c_{i_1,k+1}\right). \tag{49}$$

The 3D implementation requires the selection of an appropriate support for the interpolation in the plane. As in the previous case, let us assume a solid surface defined by the plane plane $z = \text{const}$, where solid nodes have constant index k and the first fluid layer is at $k+1$. Also, the lattice nodes in the planes parallel to the solid surface are addressed by the indices i and j. The location of the interpolating points is determined by the gradients of the concentration field in the plane $l_x = l_\parallel \nabla_x c/|\nabla c_\parallel|$ and $l_y = l_\parallel \nabla_y c/|\nabla c_\parallel|$. The simplest interpolation scheme for a plane in 3D requires three points. In our implementation we select the three furthest points (of four) from the location (i, j) in a planar square lattice (cfr. the sketch in Fig. 9(b).

Once the three points are selected, we consider the three triplets (x_1, y_1, c_1), (x_2, y_2, c_2), and (x_3, y_3, c_3), describing a plane, where the third coordinate represents the value of the concentration c in each point. The following interpolation scheme is employed to compute the field values in the ghost

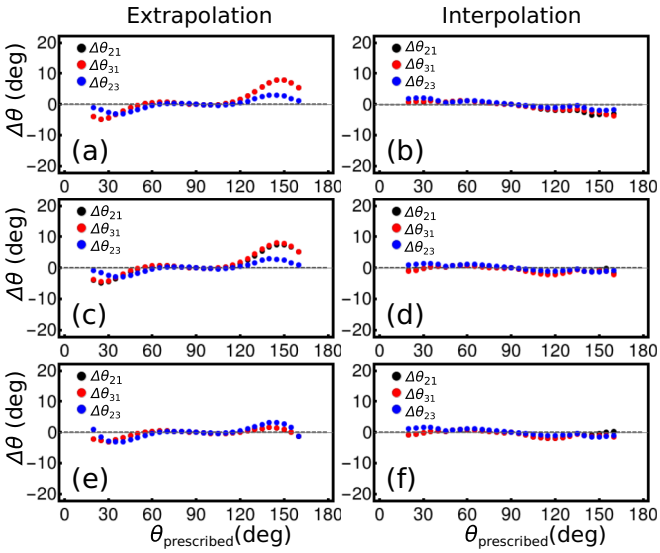

FIG. 10. Deviation of contact angles θ_{21}, θ_{31} and θ_{23}, measured on sessile drops in mechanical equilibrium from the prescribed values. Results for the *geometric extrapolation* method (left column) and the *geometric interpolation* method (right column). The interfacial properties correspond to set 1 (first row), set 2 (second row), and set 3 (first row) listed in Table I.

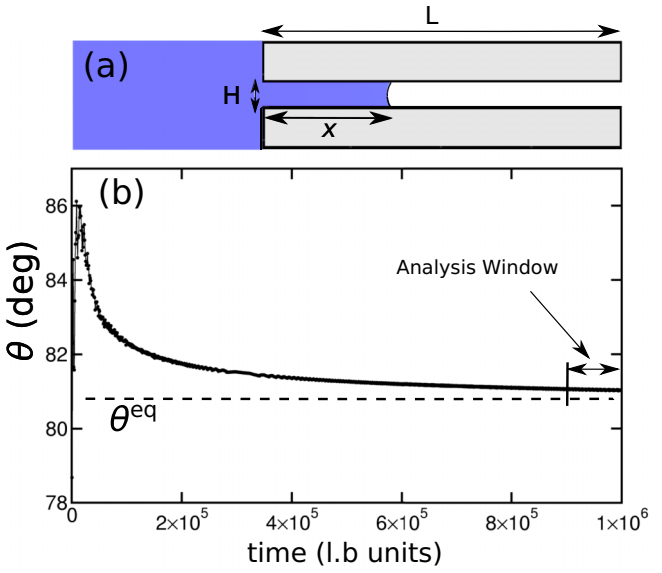

FIG. 11. Capillary filling: (a) Sketch of the simulation setup; (b) dynamic contact angle vs. simulation time for the *Geometric Interpolation* method and $\theta_{21} = 80°$. The analysis window consists of the last 10% of the simulation time, over which the dynamic contact angle is averaged.

node located in (i, j, k):

$$c_{i,j,k} = \frac{Al_x + Bl_y + C}{D}, \tag{50}$$

where A, B, C, D are the polynomials

$$\begin{aligned} A &= y_2c_1 - y_3c_1 - y_1c_2 + y_3c_2 + y_1c_3 - y_2c_3 \\ B &= -x_2c_1 + x_3c_1 + x_1c_2 - x_3c_2 - x_1c_3 + x_2c_3 \\ C &= -x_3y_2c_1 + x_2y_3c_1 + x_3y_1c_2 \\ &\quad - x_1y_3c_2 - x_2y_1c_3 + x_1y_2c_3 \\ D &= -x_2y_1 + x_3y_1 + x_1y_2 - x_3y_2 - x_1y_3 + x_2y_3. \end{aligned} \tag{51}$$

We have assessed the accuracy of both geometric methods by simulating sessile drops in mechanical equilibrium for each fluid-fluid interface and comparing the parameter sets 1, 2, and 3 in Table I. The simulation setup and analysis are the same as previously employed to validate the force method, as shown in Fig. 10. In the intermediate range of angles [60°, 120°] both methods show good agreement, with deviations below 1°, while for larger and smaller angles the *geometry interpolation* method is to be preferred. In view of this result, we discard the *extrapolation* in favour of the *interpolation* method for the remaining tests.

At this point, it is also useful to note that the Girifalco-Good relation in Eq. (45) is not immediately satisfied for the geometric approaches. This is because the contact angle between any two fluids and a solid surface can be arbitrarily assigned, unlike the force method where the thermodynamic consistency is guaranteed. To respect thermodynamic consistency, one should therefore ensure the choice of contact angles in the implementations of geometric approaches should satisfy the Girifalco-Good relation, Eq. (45). We will take advantage of the freedom of choosing arbitrary combinations of contact angles to simulate self propelled bislugs in a channel in Sec. VI.

V. CAPILLARY FILLING

To assess the dynamic properties of fluid interfaces, we simulate the capillary filling of a channel by a liquid. The problem was studied independently by Richard Lucas [58] and Edward Washburn [59]. It represents a classical benchmark for wetting boundary conditions in lattice Boltzmann implementations [60–62], as it provides analytical or semi-analytical expressions to compare.

Let us now consider the system sketched in Fig. 11, consisting in a 2D channel of height H, initially containing a gas phase only, and filled by liquid. The liquid-gas surface tension is denoted by γ, while the liquid forms a contact angle θ with the solid.

In a 2D geometry, the driving capillary force is applied at the two contact points of the liquid interface with the channel walls:

$$F^{\text{cap}} = 2\gamma \cos\theta. \tag{52}$$

Except for the initial transient time, the resisting force is mainly provided by viscous dissipation. In virtue of the high density ratio in our model, we neglect the dissipation in the gas phase [63]. For a liquid of viscosity $\mu = \rho_l \nu$ forming a column of length x, and assuming a fully developed Poiseuille velocity profile, we have a resisting force,

$$F^{\text{visc}} = -\frac{12\rho_l \nu x \dot{x}}{H}, \tag{53}$$

where $\dot{x}$ is the mean velocity of the fluid column, corresponding to the velocity of the liquid-gas interface. Equations (52)

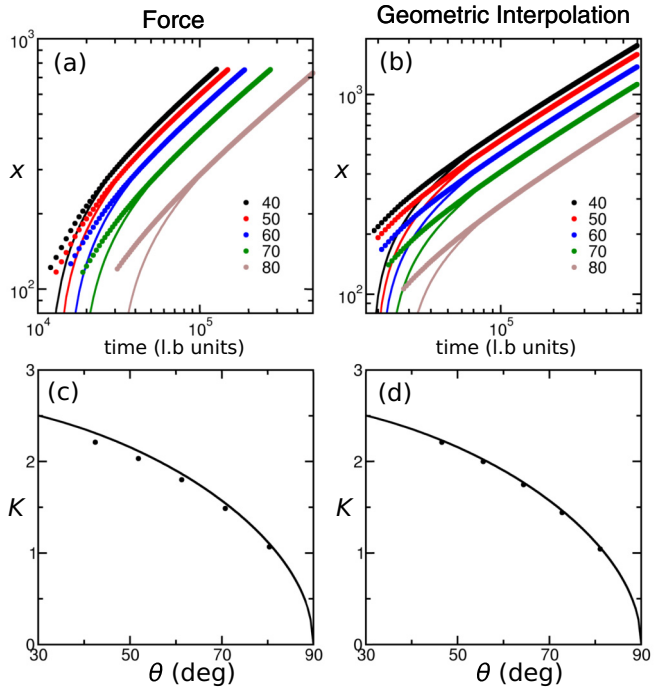

FIG. 12. Capillary filling: [(a) and (b)] Length of the liquid column vs. simulation time for contact angles $\theta = 40^\circ, 50^\circ, 60^\circ, 70^\circ$, and 80°. Dots represent numerical results, while continuous lines data fits. [(c) and (d)] Prefactor K for the Lucas-Washburn law. Dots represent fits to the numerical results, and the continuous line is the model prediction [Eq. (55)]. Left panels [(a) and (c)] are obtained employing the force method, while right panels [(b) and (d)] are obtained employing the geometric interpolation method.

and (53) lead to the so-called Washburn law,

$$x(t) = K\sqrt{(t - t_0)}, \tag{54}$$

where t_0 is a time constant. The prefactor

$$K = \sqrt{\frac{\gamma \cos\theta H}{3\nu\rho_l}} \tag{55}$$

is function of material and geometric parameters only: the surface tension γ, the equilibrium contact angle θ, the kinematic viscosity ν of the liquid, and channel height H.

In our simulations the channel length is $L = 2000$ l.u. and the height $H = 70$ l.u. The channel is preceded and followed by reservoirs filled with liquid and gas, respectively. This geometry has been previously employed [63] to minimize the viscous drag of the fluid outside the channel. Throughout all simulations we employ the first parameter set in Table I, for which $\gamma = 0.414$ in both liquid-gas interfaces, and set $\beta = 0.5$, giving a kinematic viscosity $\nu = 1/6 = 0.16667$.

In Figs. 12(a) and 12(b) we report the time evolution of the front of the liquid column for contact angles varied in the range of $[30^\circ, 80^\circ]$, comparing the *force* and *geometric interpolation* methods. The initial stage of the invasion is not well described by Washburn's law [63]. As shown in Fig. 11(b), during the filling process the dynamic angle varies over time and approaches the equilibrium value only asymptotically. Consequently, Washburn's law [Eq. (54)] describes accurately only the asymptotic regime, while for the initial and transient regimes inertia and viscous bending should also be considered.

As in this specific test our main interest is comparing the accuracy of the *force* and *geometric interpolation* methods, we analyze the last 10% of the simulation time, where the variation of dynamic angles are below one degree, and we can assume Eq. (54) to be sufficiently accurate. To eliminate systematic sources of errors, we compute the average dynamic angle $\langle\theta\rangle$ within the analysis window and replace with it the angle θ in Eq. (55). Furthermore, we perform a parametric fit of the numerical data within the analysis window with Eq. (54) and compute the time constant t_0 and the prefactor K.

In Figs. 12(c) and 12(d) we compare the values of K to the model [Eq. (55)]. The data for the *force* method show small deviations between predicted and measured values of the prefactor. The deviations increase proportionally with the magnitude of the forcing term, which increases as θ decreases. This suggests that the discrepancy is related to spurious velocities near the walls, due the force term in the *force* method. In contrast, we observe no deviations for the *geometric interpolation*.

VI. SELF-PROPELLED SLUGS

In this section we focus on a ternary-specific benchmark, consisting in a self-propelled train of drops (bislug) in a 2D channel.

In experiments, a bislug with three finite contact angles cannot self-propel, unless the Girifalco-Good relation, Eq. (45), is broken. This may be done by introducing a step or gradient of wettability on the channel surfaces [64,65]. Alternatively, at least one liquid phase must be completely wetting. This last condition was exploited by Bico and Queré to study experimentally in detail self propelled bislugs [66,67]. Taking advantage of the *geometric interpolation* method, we can numerically introduce arbitrary contact angles in the system providing a controlled mechanism for self-propulsion.

The simulation geometry, sketched in Fig. 13(a), consists of a periodic channel of height $H = 39$ l.u. It contains a train of drops having equal volumes. For simplicity, we assume the length $L_1 = L_2$ of each liquid drop, approximated by the length of the equivalent rectangle having the same area and height H. The total length of the periodic channel is adjusted in each simulations to allow the presence of at least 200 lattice units of gas at the two sides of the bislug.

A. Bislug dynamics

In long trains of drops the driving force is almost completely dissipated in the liquid bulk. Consequently, the velocity is small and the contact angles remain close to the equilibrium value. According to the convention for contact angles employed in this work, the surface tension unbalance is expressed by

$$\Delta\gamma = \gamma_{23}\cos\theta_{23} - \gamma_{13}\cos\theta_{31} + \gamma_{12}\cos\theta_{21}, \tag{56}$$

and the driving force is

$$F^{\text{cap}} = 2\Delta\gamma, \tag{57}$$

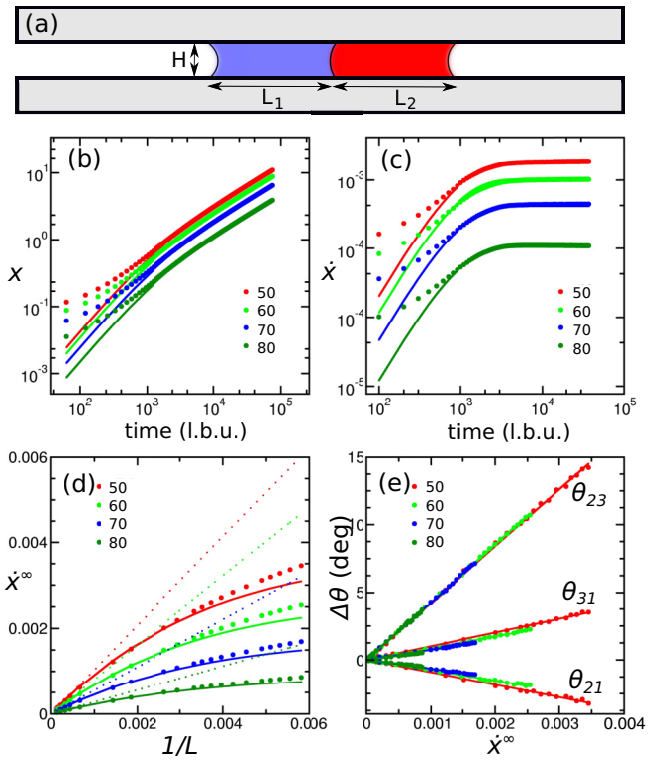

FIG. 13. Self-propelled bislugs: (a) Sketch of the simulation setup. The other panels report data for bislugs defined by the first parameter set in Table I. We set $\beta = 0.5$ and contact angles $\theta_{23} = \theta_{21} = \theta_{31} = 50^\circ, 60^\circ, 70^\circ, 80^\circ$. [(b) and (c)] Transient regime in the motion of the bislugs of length $L = 1500$ l.u., showing (b) the position and (c) the velocity of the center of mass. (d) The measured steady velocity $\dot{x}_\infty$ as function of $1/L$. (e) The dynamic contact angles for the three interfaces as function of $\dot{x}_\infty$.

Assuming a Poiseuille flow profile in the bislug and liquids with equal viscosity, the viscous force is

$$F^{\text{visc}} = -\frac{12\rho_l \nu L \dot{x}}{H}, \tag{58}$$

where $\dot{x}$ is the mean fluid velocity, associated to the velocity of the center of mass of the bislug.

In the limit of long trains ($L = L_1 + L_2 \gg H$) the viscous bending can be neglected, and the equation of motion for the center of mass is [63,64]

$$\rho_l L H \ddot{x} = F^{\text{cap}} + F^{\text{visc}}. \tag{59}$$

By introducing Eqs. (57) and (58) into Eq. (59), we obtain

$$\ddot{x} + \frac{12\nu}{H^2}\dot{x} - \frac{2\Delta\gamma}{\rho_l L H} = 0. \tag{60}$$

Integrating once with time and imposing $\dot{x}(0) = 0$, we obtain an exponential relaxation of the bislug velocity to the steady velocity v_∞,

$$\dot{x}(t) = v_\infty\left(1 - e^{\frac{-t}{\tau_{\text{rel}}}}\right), \tag{61}$$

where the steady velocity is

$$v_\infty = \frac{H\Delta\gamma}{6\rho_l \nu L} \tag{62}$$

and the relaxation time is

$$\tau_{\text{rel}} = \frac{H^2}{12\nu}. \tag{63}$$

Integrating Eq. (61) once again with time we obtain the displacement of the center of mass with respect to its initial position $x(0)$

$$x(t) = x(0) + \tau_{\text{rel}} v_\infty\left(e^{\frac{-t}{\tau_{\text{rel}}}} + \frac{t}{\tau_{\text{rel}}} - 1\right). \tag{64}$$

In the simulation we initialize the bislug as two rectangular liquid drops in the beginning of the channel. Typically, during the first 10^3 steps of the simulation, the liquid interfaces quickly deform to approach the contact angle of the steady-moving bislug and initiate the self-propulsion mechanism. In Fig. 13 we compare the trajectory [Fig. 13(b)] and velocity [Fig. 13(c)] of a long train of drops ($L = 1500$ l.u.), with Eqs. (64) and (61) for contact angles $\theta_{23} = \theta_{21} = \theta_{31}$ varied in the range $[50^\circ, 80^\circ]$. Equations (61) and (64) capture accurately the bislug dynamics after the first 10^3 time steps. A close inspection of Fig. 13(c) shows that after 10^4 time steps the bislug speed has fully reached the steady value v_∞.

In Fig. 13(d) we report the steady velocity $\dot{x}_\infty$ of the bislug as function of L^{-1} for the same combinations of contact angles. We observe that $\dot{x}_\infty \simeq v_\infty$ (dotted lines) in the limit of long bislugs, while, as the bislugs shorten, $\dot{x}_\infty$levels off, implying the importance of additional channels for energy dissipation.

To assess whether in our numerical model the additional dissipation originates predominantly from the viscous bending of the fluid interfaces, we measure dynamic angles for all the fluid interfaces, fitting the fluid interfacial profiles with circles [68]. In Fig. 13(e) we report the contact angle difference $\Delta\theta = \theta(\dot{x}_\infty) - \theta(0)$ and observe a linear dependence with the bislug speed $\dot{x}_\infty$.

Motivated by this observation, we perform linear fits and introduce the correction $\Delta\theta$ in the evaluation surface tension unbalance $\Delta\theta$, Eq. (56). The corrected model is depicted by solid lines in Fig. 13(d) and shows excellent agreement with the measured values of $\dot{x}_\infty$.

B. Contact line slip

We now further employ the numerical experiment of self-propelled bislugs to quantify the slip properties of our ternary model. While a similar analysis could be carried out also for the capillary filling, the bislug geometry has the advantage that trains of drops approach a steady motion with constant velocity, which can be measured more accurately. Furthermore, by tuning the length of the bislugs, it is possible to vary accurately the velocity in a wide range.

As shown by Briant [50,51], in multiphase lattice Boltzmann models, the main slip mechanism relies on evaporation-condensation of the liquid interface, while in multicomponent models the contact line advances in virtue of the diffusion of the phase field [68,69]. When coupling multiphase and multicomponent models, both evaporation-condensation and diffusion mechanisms occur at the liquid-gas interface. In contrast, at the liquid-liquid interface, only the diffusion mechanism is important, as the density ρ does not vary.

Following Cox's analysis [70,71], the viscous bending of a fluid interface is described by

$$g(\theta, \lambda) - g(\theta_w, \lambda) = \mathrm{Ca} \ln(L_c/L_s), \tag{65}$$

where θ is a dynamic contact angle measured at a macroscopic distance from the surface and θ_w is the equilibrium contact angle at the solid boundaries. The capillary number $\mathrm{Ca} = \mu \dot{x}_\infty/\gamma$ represents the nondimensional velocity of the interface, where the viscosity $\mu = \mu_{\mathrm{adv}}$ refers to the invading fluid. In our simulation we identify the macroscopic distance L_c with the channel height H and interpret the microscopic length L_s as an estimate for the slip length. The parameter $\lambda = \mu_{\mathrm{adv}}/\mu_{\mathrm{rec}}$ describes the ratio between the dynamic viscosity of the invading μ_{adv} and resisting μ_{res} fluids.

For liquid with equal density we have $\lambda = \nu_{\mathrm{adv}}/\nu_{\mathrm{rec}}$. Specifically, for the bislug simulations $\lambda = 1$ at the liquid-liquid interface, $\lambda \simeq 10^3$ for a liquid displacing the gas phase and $\lambda \simeq 10^{-3}$ for the gas displacing a liquid phase. The function $g(\theta, \lambda) = \int_0^\theta 1/f(\phi, \lambda) d\phi$ is a known function of θ and λ, given in Refs. [70] and [71]:

$$f(\theta) = \frac{2\sin\theta\{\lambda^2(\theta^2 - \sin^2\theta) + 2\lambda[\theta(\pi - \theta) + \sin^2\theta] + [(\pi - \theta)^2 - \sin^2\theta]\}}{\lambda(\theta^2 - \sin^2\theta)[(\pi - \theta) + \sin\theta\cos\theta] + [(\pi - \theta)^2 - \sin^2\theta](\theta - \sin\theta\cos\theta)}. \tag{66}$$

To systematically explore the slip properties, we perform simulations for two sets of contact angles. In the first set we fix $\theta_{23} = 60^\circ$ and vary systematically $\theta_{21} = \theta_{31}$ in the range $[50^\circ, 120^\circ]$. In the second set we fix $\theta_{21} = \theta_{31} = 90^\circ$ and vary systematically θ_{23} in the range $[30^\circ, 150^\circ]$. The first set allows us to extract information for the liquid-gas interfaces, while the second set for the liquid-liquid interface.

For each combination of contact angles we simulate the motion of bislugs for a wide range of lengths and speeds. Furthermore, we compute the capillary length Ca of the advancing fluid (which can be either a liquid or the gas phase, depending the interface considered) and evaluate the Cox function $g(\theta)$ in Eq. (65) for the appropriate value of viscosity contrast λ. Due to the limited variation of the dynamic contact angles (in a range of a few degrees), for simplicity we perform a linear regression to evaluate the slope $m = \partial g(\theta)/\partial \mathrm{Ca} = \ln(L_c/L_s)$. Finally, introducing the geometric parameter $L_c = H = 39$, we estimate the slip length as $L_s = L_c \exp(-m)$.

In Fig. 14, we compare L_s for the three interfaces as a function of the equilibrium contact angle. More specifically, for our geometry we obtain θ_{21} (receding), θ_{31} (advancing), and θ_{23} (advancing for $\theta_{23} < 90^\circ$ and receding for $\theta_{23} > 90^\circ$). The slip length for the liquid-liquid interface shows a minimum for $\theta_{23} = 90^\circ$ (the data point is not present, because for this combination of angles we have no net driving force $\Delta\gamma = 0$) and increases symmetrically for larger and smaller angles. In contrast the slip length for the liquid-gas interfaces shows a monotonic decrease as the equilibrium contact angle increases. For the last available data point, at $\theta = 120^\circ$, L_s is similar for all three interfaces, while for smaller angles L_s is significantly larger for the liquid-gas interfaces.

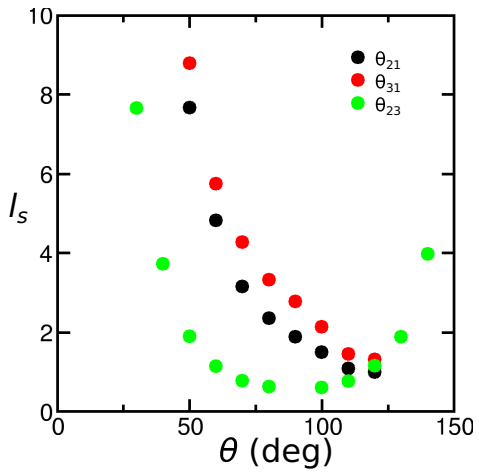

FIG. 14. Estimated slip length vs. equilibrium contact angle for the liquid-liquid and the liquid-gas interfaces.

These results show that the slip properties in the system strongly depend on the nature of the fluid-fluid interface. In our tests the liquid-gas interfaces present a larger slip length (up to a factor 4) compared to the liquid-liquid interface, likely due to the combined effect of two distinct mechanisms operating on the density ρ and the field ϕ.

VII. DISCUSSION AND CONCLUSIONS

In this work we have thoroughly benchmarked our ternary high-density-ratio free-energy model and provided guidelines to select the free-energy parameters for obtaining a wide range of surface tension combinations. We have quantified the deviations of the interface profile by measuring the "concentration deviation coefficient" and systematically investigated eight subspaces, covering relevant combinations of parameters. All data are reported in the Supplemental Material [52], including fitting functions to estimate the surface tensions.

We have compared three methods for wetting of solid boundaries, namely force, geometric extrapolation, and geometric interpolation. Of the two geometric methods, geometric interpolation is significantly more accurate. The force method provides a useful alternative to geometric methods, as it does not require us to detect the fluid interface *a priori* and automatically satisfies the Girifalco-Good relation, Eq. (45).

The benchmark on the dynamics of capillary filling shows that the force method is slightly less accurate than the geometric methods. The deviations in the measured prefactor of the Washburn law increase as the material contact angles depart from neutral wetting. Because the additional force terms also increase, we expect that the deviations are related to additional spurious velocities generated by the forcing terms. At the same time no spurious velocities are observed in the geometric methods.

Furthermore, we have performed a ternary specific benchmark and studied the motion of self-propelled bislugs forming three finite and unbalanced contact angles. The analytic model for the bislug motion, derived by assuming equilibrium values for the contact angles, accurately captures the linear dependence of steady-state velocities from the inverse of the bislug length for long trains of drops and small velocities. The level-off of the velocity experimentally observed for shorter bislugs is captured in our simulations by accounting for the dynamic angle correction in the driving force. The agreement shows that the viscous bending of the liquid interfaces represents the main correction in the model.

Finally, we have shown that coupling multiphase and multicomponent models leads to significant differences in the slip properties of liquid-liquid and liquid-gas interfaces. While for liquid-liquid interfaces the only slip mechanism is related to the diffusion of the field ϕ, for liquid-gas interfaces the slip mechanism combines the diffusion of the field ϕ and the evaporation-condensation of the density ρ.

In our tests, at parity of interfacial properties, the slip length varies with the material contact angle and is generally larger for the liquid-gas interfaces than for the liquid-liquid interfaces. A more detailed analysis of the slip properties of the system will be the subject of a future investigation.

ACKNOWLEDGMENTS

N.B. gratefully acknowledges financial support from University of Northumbria at Newcastle via a Postgraduate Research Studentship. I.K. acknowledges support by European Research Council (ERC) Advanced Grant No. 834763-PonD and by Swiss National Science Foundation (SNF) Grant No. 200021_172640. H.K. thanks Procter & Gamble and EPSRC for funding (Grant No. EP/P007139/1). C.S. acknowledges support from Northumbria University through the Vice-Chancellor's Fellowship Programme.

[1] A. S. Utada, E. Lorenceau, D. R. Link, P. D. Kaplan, H. A. Stone, and D. A. Weitz, Science (NY) **308**, 537 (2005).
[2] C. Planchette, E. Lorenceau, and G. Brenn, Fluid Dyn. Mat. Proc. **7**, 279 (2011).
[3] C. Planchette, S. Petit, H. Hinterbichler, and G. Brenn, Phys. Rev. Fluids **3**, 093603 (2018).
[4] C. H. Wang, C. Z. Lin, W. G. Hung, W. C. Huang, and C. K. Law, Combust. Sci. Technol. **176**, 71 (2004).
[5] L. Changlin-lin, L. Xin-wei, Z. Xiao-liang, L. Ning, D. Hongna, W. Huan, and L. Yong-ge, in *Proceedings of the SPE Asia Pacific Oil and Gas Conference and Exhibition*, Vol. 2 (Society of Petroleum Engineers, 2013).
[6] D. W. Murphy, C. Li, V. D'Albignac, D. Morra, and J. Katz, J. Fluid Mech. **780**, 536 (2015).
[7] J. D. Smith, R. Dhiman, S. Anand, E. Reza-Garduno, R. E. Cohen, G. H. McKinley, and K. K. Varanasi, Soft Matter **9**, 1772 (2013).
[8] A. Keiser, L. Keiser, C. Clanet, and D. Quéré, Soft Matter **13**, 6981 (2017).
[9] H. Hua, J. Shin, and J. Kim, Int. J. Heat Fluid Flow **50**, 63 (2014).
[10] B. Merriman, J. K. Bence, and S. J. Osher, J. Comput. Phys. **112**, 334 (1994).
[11] P. Gao and J. J. Feng, J. Fluid Mech. **682**, 415 (2011).
[12] J. Kim, Commun. Comput. Phys. **12**, 613 (2012).
[13] C.-Y. Zhang, H. Ding, P. Gao, and Y. L. Wu, J. Comput. Phys. **309**, 37 (2016).
[14] R. Haghani Hassan Abadi, M. H. Rahimian, and A. Fakhari, J. Comput. Phys. **374**, 668 (2018).
[15] J. M. Park, Appl. Math. Comput. **330**, 11 (2018).
[16] S. Succi, *The Lattice Boltzmann Equation: For Fluid Dynamics and Beyond* (Oxford University Press, Oxford, 2001).
[17] T. Krüger, H. Kusumaatmaja, A. Kuzmin, O. Shardt, G. Silva, and E. M. Viggen, *The Lattice Boltzmann Method: Principles and Practice* (Springer, New York, 2016).
[18] H. Kusumaatmaja, J. Léopoldès, A. Dupuis, and J. M. Yeomans, Europhys. Lett. **73**, 740 (2006).
[19] H. Kusumaatmaja and J. M. Yeomans, Langmuir **23**, 6019 (2007).
[20] R. Ledesma-Aguilar, R. Nistal, A. Hernández-Machado, and I. Pagonabarraga, Nat. Mater. **10**, 367 (2011).
[21] A. E. Komrakova, O. Shardt, D. Eskin, and J. J. Derksen, Int. J. Multiphase Flow **59**, 24 (2014).
[22] K. N. Premnath and J. Abraham, Phys. Fluids **17**, 122105 (2005).
[23] A. Mazloomi Moqaddam, S. S. Chikatamarla, and I. V. Karlin, J. Stat. Phys. **161**, 1420 (2015).
[24] A. M. Moqaddam, S. S. Chikatamarla, and I. V. Karlin, Phys. Fluids **28**, 022106 (2016).
[25] A. Montessori, P. Prestininzi, M. La Rocca, and S. Succi, Phys. Fluids **29**, 092103 (2017).
[26] S. Mukherjee and J. Abraham, J. Colloid Interface Sci. **312**, 341 (2007).
[27] T. Lee and L. Liu, J. Comput. Phys. **229**, 8045 (2010).
[28] A. Banari, C. F. Janßen, and S. T. Grilli, Comput. Math. Appl. **68**, 1819 (2014).
[29] K. Ashoke Raman, R. K. Jaiman, T. S. Lee, and H. T. Low, Chem. Eng. Sci. **145**, 181 (2016).
[30] Y. Liu, M. Andrew, J. Li, J. M. Yeomans, and Z. Wang, Nat. Commun. **6**, 10034 (2015).
[31] M. Andrew, Y. Liu, and J. M. Yeomans, Langmuir **33**, 7583 (2017).
[32] M. Sbragaglia, L. Biferale, G. Amati, S. Varagnolo, D. Ferraro, G. Mistura, and M. Pierno, Phys. Rev. E **89**, 012406 (2014).
[33] A. Mazloomi Moqaddam, S. S. Chikatamarla, and I. V. Karlin, J. Fluid Mech. **824**, 866 (2017).
[34] R. D. M. Travasso, G. A. Buxton, O. Kuksenok, K. Good, and A. C. Balazs, J. Chem. Phys. **122**, 194906 (2005).
[35] T. J. Spencer, I. Halliday, and C. M. Care, Phys. Rev. E **82**, 066701 (2010).
[36] K. S. Ridl and A. J. Wagner, Phys. Rev. E **98**, 043305 (2018).
[37] C. Semprebon, T. Krüger, and H. Kusumaatmaja, Phys. Rev. E **93**, 033305 (2016).

[38] C. Semprebon, G. McHale, and H. Kusumaatmaja, Soft Matter **13**, 101 (2017).
[39] M. S. Sadullah, C. Semprebon, and H. Kusumaatmaja, Langmuir **34**, 8112 (2018).
[40] A. Mazloomi M, S. S. Chikatamarla, and I. V. Karlin, Phys. Rev. Lett. **114**, 174502 (2015).
[41] H. Liang, J. Xu, J. Chen, Z. Chai, and B. Shi, App. Math. Mod. **73**, 487 (2019).
[42] Y. Shi, G. H. Tang, and Y. Wang, J. Comput. Phys. **314**, 228 (2016).
[43] Y. Wang, C. Shu, H. B. Huang, and C. J. Teo, J. Comput. Phys. **280**, 404 (2015).
[44] M. Wöhrwag, C. Semprebon, A. Mazloomi Moqaddam, I. Karlin, and H. Kusumaatmaja, Phys. Rev. Lett. **120**, 234501 (2018).
[45] S. S. Chikatamarla, S. Ansumali, and I. V. Karlin, Phys. Rev. Lett. **97**, 010201 (2006).
[46] P. Yuan and L. Schaefer, Phys. Fluids **18**, 042101 (2006).
[47] A. Mazloomi M., S. S. Chikatamarla, and I. V. Karlin, Phys. Rev. E **92**, 023308 (2015).
[48] I. V. Karlin, A. Ferrante, and H. C. Öttinger, Europhys. Lett. **47**, 182 (1999).
[49] S. Ansumali, I. V. Karlin, and H. C. Öttinger, Europhys. Lett. **63**, 798 (2003).
[50] A. J. Briant and J. M. Yeomans, Phys. Rev. E **69**, 031603 (2004).
[51] A. J. Briant, A. J. Wagner, and J. M. Yeomans, Phys. Rev. E **69**, 031602 (2004).
[52] See Supplemental Material at http://link.aps.org/supplemental/10.1103/PhysRevE.100.013308 for two dimensional plots of surface tensions, Neumann angles, spreading parameter and concentration deformation factor for 8 sub-spaces of the six dimensional free energy parameter space. Polynomial fitting function for the surface tension of each interface are included.
[53] A. J. C. Ladd, J. Fluid Mech. **271**, 285 (1994).
[54] H. Huang, D. T. Thorne, M. G. Schaap, and M. C. Sukop, Phys. Rev. E **76**, 066701 (2007).
[55] L. Girifalco and R. Good, J. Phys. Chem. **61**, 904 (1957).
[56] H. Ding and P. D. M. Spelt, Phys. Rev. E **75**, 046708 (2007).
[57] H. G. Lee and J. Kim, Comp. Fluids **44**, 178 (2011).
[58] R. Lucas, Kolloid-Zeitschrift **23**, 15 (1918).
[59] E. W. Washburn, Phys. Rev. **17**, 273 (1921).
[60] H. S. Wiklund, S. B. Lindström, and T. Uesaka, Comput. Phys. Commun. **182**, 2192 (2011).
[61] H. Liu, Y. Ju, N. Wang, G. Xi, and Y. Zhang, Phys. Rev. E **92**, 033306 (2015).
[62] Q. Lou, M. Yang, and H. Xu, Commun. Comput. Phys. **23**, 1116 (2018).
[63] F. Diotallevi, L. Biferale, S. Chibbaro, A. Lamura, G. Pontrelli, M. Sbragaglia, S. Succi, and F. Toschi, Eur. Phys. J.: Spec. Top. **166**, 111 (2009).
[64] E. Esmaili, A. Moosavi, and A. Mazloomi, J. Stat. Mech. (2012) P10005.
[65] J.-J. Huang, H. Huang, and X. Wang, Phys. Fluids **26**, 062101 (2014).
[66] J. Bico and D. Quéré, Europhys. Lett. **51**, 546 (2000).
[67] J. Bico and D. Quéré, J. Fluid Mech. **467**, 101 (2002).
[68] H. Kusumaatmaja, E. J. Hemingway, and S. M. Fielding, J. Fluid Mech. **788**, 209 (2016).
[69] D. Jacqmin, J. Fluid Mech. **402**, 57 (2000).
[70] R. G. Cox, J. Fluid Mech. **168**, 195 (1986).
[71] R. G. Cox, J. Fluid Mech. **357**, 249 (1998).